Biosensors and Bioelectronics 123 (2019) 7–13

Contents lists available at ScienceDirect

Biosensors and Bioelectronics

journal homepage: www.elsevier.com/locate/bios

Boosted photoelectrochemical immunosensing of metronidazole in tablet using coral-like g-C_3N_4 nanoarchitectures

Xin Li, Yijin Yuan, Xinmeng Pan, Lizhi Zhang, Jingming Gong*

Key Laboratory of Pesticide & Chemical Biology of Ministry of Education, College of Chemistry, Central China Normal University, Wuhan 430079, PR China

ARTICLE INFO

Keywords:
Photoelectrochemical immunoassay
Coral-like g-C_3N_4
Metronidazole
Oral medicine sample
Nanoarchitectured design

ABSTRACT

A simple, facile and sensitive photoelectrochemical (PEC) bioassay protocol for metronidazole (MNZ) detection in common oral medicine samples has been proposed under visible-light irradiation, where novel hierarchical coral-like g-C_3N_4 nanoarchitectures (cg-C_3N_4) have been first explored as PEC sensing platform. Featured with the unique nanostructures (e.g., interlaced porous network architecture, and open boundaries), the as-formed cg-C_3N_4 nanoarchitectures not only efficiently inhibit the recombination of photogenerated electron-hole but also enable the immobilization of capture antibodies as well as the antibody-antigen binding efficiency fluently, thus amplifying the photocurrent response. This newly constructed PEC immunoassay displays excellent performance for MNZ determination with high sensitivity and selectivity. Under the optimal condition, this bioassay protocol exhibits a linear range of 0.01–100 μM with a detection limit of 0.005 μM at signal to noise ratio of 3. The resulting PEC immunoassay has been proved to be applicable for sensing MNZ in common oral medicine samples.

1. Introduction

Metronidazole (MNZ, 1-(2-hydroxyethyl)-2-methyl-5-nitroimidazole) has been widely used as antibacterial and antiprotozoa medicine (Chen et al., 2013; Mahrouse and Elkady, 2011). Generally, it is used in the treatment of anti-anaerobic infections, follicle worms, amebiasis, giardiasis, tichomoniasis and periodontal disease. However, MNZ has been evidenced to have genotoxic, carcinogenic and mutagenic side effects (Mehrzad-Samarin et al., 2017; Thompson et al., 2009). Hence, the determination of trace residues of MNZ in different matrixes has aroused much concern. Several methods, including high-performance liquid chromatography (HPLC) (Ardsoongnearn et al., 2014; Schkarpetkin et al., 2016; Wang et al., 2012), thin-layer chromatography (TLC) (Moussa et al., 2017), spectrophotometry (Korany et al., 2015; Zheltvai et al., 2013) and electrochemical sensor (Song et al., 2016) have been utilized for MNZ determination. However, most of these methods are often subjected to deficiency in simplicity, cost-effectiveness and portability. Therefore, to develop a facile and sensitive protocol for rapid detection of MNZ is urgent.

In recent years, with outstanding advantages of high sensitivity, cost efficiency, ease of operation, and inherent miniaturization, photoelectrochemical (PEC) immunoassays have attracted great attention with intrinsic separation for the excitation source / detection signal (Dai et al., 2016; Shen et al., 2015; Shu et al., 2016). Nowadays, great efforts have been made on improving the sensitivity for PEC detection of low-abundance biomarker proteins (Ge et al., 2014; Li et al., 2017; X. Li et al., 2018; Zhao et al., 2012). Most reported PEC assays mainly focused on nanoarchitectured designing the photoactive materials-based sensing platform with excellent photon-to-electron conversion efficiency, good electrical conductivity, and high surface area (Gao et al., 2017; Wang et al., 2017).

Recently, graphitic-like carbon nitride (g-C_3N_4) has aroused widespread attention due to its appealing electronic band structure, earth-abundant nature, high stability, and visible-light absorption ability (Liao et al., 2012; Wang et al., 2015; Zheng et al., 2014). It has been used on catalysis (Hou et al., 2013; Lu et al., 2017; S. Yang et al., 2013; Yu et al., 2014), degradation (Liu et al., 2018; Xie et al., 2018; Y. Yang et al., 2013; Yue et al., 2018), and sensing probes (Chen et al., 2015; Duan et al., 2018; Fang et al., 2016; Liu et al., 2016). Nevertheless, some intrinsic nature (e.g. the rapid recombination speed of photogenerated h^+-e^- pair, low quantum efficiency and surface area) strongly hampered its practical applications. Thus, to overcome these problems, several attempts have been made, including nanostructure synthesis (Hou et al., 2013; Ma et al., 2014), doping foreign elements (Fan et al., 2018; Han et al., 2018), and coupling with typical semiconductors to form heterojunctions (H. Li et al., 2018; Sun et al., 2015). In particular,

* Corresponding author.
E-mail address: jmgong@mail.ccnu.edu.cn (J. Gong).

https://doi.org/10.1016/j.bios.2018.09.084
Received 3 July 2018; Received in revised form 11 September 2018; Accepted 24 September 2018
Available online 25 September 2018
0956-5663/

nanostructure synthesis, i.e. manipulation of nanostructured g-C_3N_4 with controllable morphologies have been proven to be an efficient protocol to improve the properties of original g-C_3N_4 (Hou et al., 2013; Ma et al., 2014). For example, recently, a soft-templating approach using hydrogen-bonded-based supramolecular network precursor has been found to be feasible to tailor g-C_3N_4 nanostructures, including g-C_3N_4 hollow nanospheres (Jun et al., 2013), nanofibers (Xie et al., 2016) and nanowires (Xie et al., 2016) with enhanced photoactivity. Inspired by this, herein, novel hierarchical coral-like g-C_3N_4 nanoarchitectures (cg-C_3N_4) are first prepared via a soft-templating approach using a cyanuric chloride-melamine (CCM) supramolecular precursor and their applications are further explored as PEC immunosensing platform for sensing MNZ. Benefitting from the unique nanostructures, such as interlaced porous network architecture and high surface area, the obtained cg-C_3N_4 nanoarchitectures facilitate the separation of the photogenerated electron-hole pair and enable the immobilization of capture antibodies as well as the antibody-antigen binding efficiency fluently, thus amplifying the photocurrent response. Such a newly constructed PEC immunoassay displays excellent performance for MNZ determination with high sensitivity and selectivity. The obtained detection limit is 0.005 μM (S/N = 3), which is significantly lower than those reported using HPLC (5.85 μM) (Wang et al., 2012), spectrophotometry (2.4 μM) (Korany et al., 2015), capillary electrophoresis (0.4 μM) (Jin et al., 2000), and electrochemical sensor (0.016 μM) (Chen et al., 2013). To the best of our knowledge, there is no report on developing hierarchical cg-C_3N_4 nanoarchitectures for PEC sensing MNZ before. The resulting PEC immunoassay is applicable for sensing MNZ in common oral medicine samples.

2. Experimental section

2.1. Materials and apparatus

All chemicals and related instruments used in the experiments have been described in Supporting information.

2.2. Synthesis of coral-like g-C_3N_4nanoarchitectures

Coral-like g-C_3N_4nanoarchitectures were synthesized by soft-template hydrothermal method. Typically, cyanuric chloride (2.7675 g) and melamine (0.9460 g) were firstly dissolved in acetonitrile (60 mL) to prepare the complex precursor cyanuric chloride-melamine (CCM) and then kept stirring overnight. Through rotary evaporation at 80 ℃ in a fuming hood, the generated white CCM precursors were redispersed in acetonitrile (80 mL). After stirring for 30 min, the mixture was transferred into a Teflon-lined autoclave (100 mL), and heated at 180 ℃ for 24 h. Followed that, the obtained samples were cleaned sufficiently with absolute alcohol, heated at 80 ℃ for overnight, then placed in a porcelain boat with a 5 cm × 6 cm ceramic chip covered and heated to 500 ℃ (10 ℃ per min) for 1 h under nitrogen atmosphere. Finally, the resulting coral-like g-C_3N_4 powders were obtained by grinding. By contrast, the bulk g-C_3N_4 was also prepared as in our previous work (Chen et al., 2015; Fang et al., 2016).

2.3. PEC immunoassay fabrication

The basal FTO substrate (with the surface area = 1.5 cm^2) was firstly washed by ultrasonicating in water and alcohol, respectively. Then, a certain amount of cg-C_3N_4 dispersion (10.0 mg mL^{-1}) was precasted on the cleaned FTO surface and stored at room temperature till dry. After that, the cg-C_3N_4/FTO surface was coated with 20 μL of CS solution (0.1 wt%) and dried at room temperature. Then, 20 μL of GLD solution (1%), a typical covalent binding agent, was further modified onto the surface of cg-C_3N_4/FTO electrode and remained for 30 min (labeled as GLD-CS/cg-C_3N_4/FTO). After rinsing, 30 μL of mAb (0.1 mg mL^{-1}, in 0.1 M PBS) was incubated on the surface of the modified electrode at 4 °C overnight (labeled as Ab/GLD-CS/cg-C_3N_4/FTO). To block any nonspecific binding sites, after rinsing, the modified electrode was further immersed in BSA solution (1%, in pH = 7.4 Tris-HCl) for 1 h. Finally, the resulting immunosensor was rinsed with washing solution (pH = 7.4 Tri-HCl with 0.05% Tween 20) and remained at 4 °C for further use (designed as BSA/Ab/GLD-CS/cg-C_3N_4/FTO). Thorough rinsing with wash solution was required at each assembly step. For comparison, 30 μL of the bulk g-C_3N_4 dispersion (10.0 mg mL^{-1}) was also coated on the cleaned surface of FTO under the same conditions (g-C_3N_4/FTO).

2.4. PEC measurements

Photocurrent measurements were accomplished in 0.1 M Tris–HCl (pH = 7.0) using AA (0.1 M) as hole scavenger before and after the incubation of BSA/Ab/GLD-CS/cg-C_3N_4/FTO into MNZ solution for an optimized time of 30 min (MNZ/BSA/Ab/GLD-CS/cg-C_3N_4/FTO), respectively. The application potential sets on 0.0 V, switch the light source every 15S.

3. Results and discussion

3.1. Characterization of Coral-like g-C_3N_4

The SEM image of the obtained cg-C_3N_4 was presented in Fig. 1A, displaying a coral-like morphology. The high-magnified SEM image (inset of Fig. 1A) reveals that the coral-like nanostructures are composed of the randomly oriented and intertwined nanorods with diameter ~40 nm. Obviously, the as-formed specific core-like g-C_3N_4 arrays, featured with interlaced porous nanoarchitecture and open boundaries with more active sites exposed, are expected to possess more efficient visible-light activity for the PEC detection (Ong et al., 2016; Zheng et al., 2014). Fig. 1B displays the typical XRD results of the bulk g-C_3N_4 and cg-C_3N_4. Two peaks at 13.0° and 27.4° are assigned to the crystal planes of (100) and (002) of g-C_3N_4 (JCPDS 87-1526), respectively (Chen et al., 2015; Fang et al., 2016). Compared with the bulk g-C_3N_4, the peak at ~ 27.4° becomes broader with a decreased intensity, mainly due to the decreased length of interlayer periodicity of cg-C_3N_4. Notably, the interconnected naonostructures of the coral-like g-C_3N_4 enable the significant decrement of the correlation length of interlayer periodicity of tri-s-triazine building blocks, showing good agreement with the previous reports (Liang et al., 2015). The FTIR spectra were collected to further characterize the structure of cg-C_3N_4. As illustrated in Fig. 1C, both spectra of cg-C_3N_4 and g-C_3N_4 display several typical bands in the range of 1200–1650 cm^{-1} (curve b), due to the typical stretching vibration modes of heptazine heterocyclic ring (C_6N_7) units (Lu et al., 2015; Yu et al., 2014). In comparison with that of g-C_3N_4, the bands within the range of 3000–3500 cm^{-1} become broadened, due to the stretching vibration of NH and NH_2 groups, confirming the presence of the amino groups in the cg-C_3N_4. In addition, the band at ~ 808 cm^{-1} was also investigated, corresponding to the breathing mode of triazine units (Lu et al., 2015).

In order to further characterize the chemical composition of the resulting products, XPS measurements were carried out (Fig. 1D). It can be seen that the cg-C_3N_4 was mainly composed of carbon and nitrogen (curve a), where the N/C ratio equals to 1.40, very close to the ideal value (N/C = 1.33) of g-C_3N_4 composition (S. Yang et al., 2013). A small amount of oxygen observed might be aroused from surface adsorption of oxygen. The high contents of carbon and nitrogen elements confirm high purity of the as-prepared cg-C_3N_4. The high-resolution spectra of C 1s and N 1s were shown in Fig. 1E & F, respectively. The main peak of C 1 s at 285.9 eV is corresponded to the sp2C=N bond contained in s-triazine ring. Another two peaks located at 286.9 eV and 284.3 eV are attributed to a sp2C atom, corresponding to -NH_2 and aromatic carbon atoms, respectively. Three peaks, located at 398.7, 399.5 and 403.6 eV are resolved from the peak of N 1s (Fig. 1F),

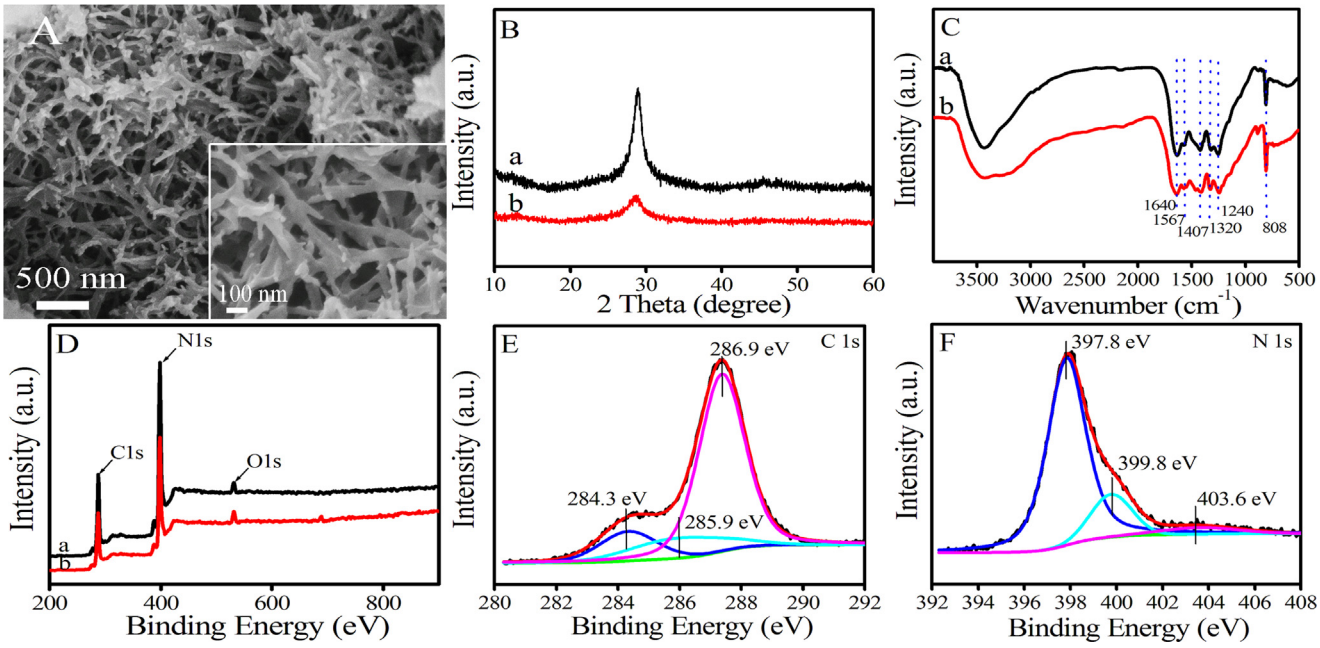

Fig. 1. (A) SEM image of the cg-C_3N_4; (B) XRD patterns,(C) FTIR spectrum and (D) XPS survey spectra of (a) g-C_3N_4 and (b) cg-C_3N_4; High-resolution XPS spectra of (E) C1s and (F) N1s of the as-prepared cg-C_3N_4. Inset of (A): the magnified image of cg-C_3N_4.

confirming that there are three kinds of nitrogen states in the resulting cg-C_3N_4 product, namely pyridinic, pyrrolic and graphitic nitrogen (Chen et al., 2015; Lu et al., 2017; Ye et al., 2015).

The UV–vis diffuse reflectance spectroscopy and photoluminescence (PL) spectrum were adopted to elucidate the optical properties of the as-prepared of cg-C_3N_4 and bulk g-C_3N_4. As shown in Fig. 2A, compared with that of bulk g-C_3N_4, an increase light absorption of cg-C_3N_4 is observed over the entire UV–vis wavelength range. The absorption edge of cg-C_3N_4 exhibits a remarkable shift from 490 nm (g-C_3N_4) to longer wavelengths of 680 nm, demonstrating enhanced absorption ability toward visible light. The plot $(\alpha h\nu)^2$ versus photo energy (inset of Fig. 2A) reveals that the band gap of the cg-C_3N_4 (~ 2.41 eV) has been narrowed by negative shift of 0.16 eV. During the solvothermal process, high mobility in the thermal fluid (acetonitrile as solvent) prompts the planar packing towards J-type aggregation of heptazine building blocks (Cui et al., 2012; Xie et al., 2016), thus improving the p-electron delocalization in conjugate system, and finally resulting in the enhancement of the absorption. The PL spectra of cg-C_3N_4 and bulk g-C_3N_4 are shown in Fig. 2B, excited by 365 nm. The strong emission peak near 440 nm is caused by direct recombination of the photogenerated electron/hole (Fang et al., 2016; Hou et al., 2013; Ma et al., 2014). The weaker PL intensity of cg-C_3N_4 demonstrates that the unique nanostructured cg-C_3N_4 could greatly decelerate the photogenerated charge carriers recombination. Seen from the photocurrent responses (Fig. 2C), a stable photocurrent of 956 nA (curve b) is obtained on cg-C_3N_4/FTO electrode, exhibiting substantial improvement compared with that of bulk g-C_3N_4/FTO (~229 nA). This indicates a notable enhancement of the charge separation at cg-C_3N_4 (curve c), showing agreement with the PL results.

According to nitrogen adsorption/desorptionisotherms, the BET surface areas of the present cg-C_3N_4 and bulk g-C_3N_4 were investigated (Fig. 2D). The cg-C_3N_4 isotherm exhibits type IV behavior with typical type H1 hysteresis loops, indicating the presence of mesoporous structure in cg-C_3N_4 (Yang et al., 2013b). While the bulk g-C_3N_4 shows a type H3 hysteresis with a typical descent in the desorption branch. The BET surface area of cg-C_3N_4 (~ 49.02 m^2/g) is found to be much greater than that of bulk g-C_3N_4 (~ 5.1 m^2/g). Obviously, the as-formed cg-C_3N_4 nanoarchitectures with enlarged surface area not only greatly facilitate the photogenerated electron-hole separation, but also provide more active sites for the further surface decoration, thereby favoring the followed PEC immunoassay applications.

3.2. Characterization of the PEC immunoassay

To verify the successful fabrication of the PEC immunoassay, the electrochemical impedance spectrum (EIS) measurements and photocurrent responses after each decoration step were conducted. The typical EIS for the electrodes after each decoration steps were show in Fig. 3A. At the bare FTO, a characteristic profile of EIS with a semicircle and a straight line has been observed, featuring a diffusion-limiting step of the $Fe(CN)_6^{4-/3-}$ (curve a). After decoration of cg-C_3N_4 on the FTO (curve b), a bigger semicircle was observed, indicating a barrier effect of semiconductor cg-C_3N_4 film on the interfacial charge transfer. The sequential immobilization of cross-linking agent (curve c), MNZ antibody (curve d), BSA (curve e) and MNZ (curve f) led to gradual increase of the semicircles, indicating the successively increased electron transfer resistance owing to the nonconductive properties of proteins. And further increasing the concentration of MNZ, the semicircle of EIS also gradually increased (curve f-h). The selective entrapment of MNZ induced the steric hindrances toward the diffusion of $[Fe(CN)_6]^{3-}$/$[Fe(CN)_6]^{4-}$ to the electrode surface, thus leading to the enhanced electron transfer resistance. With the loading of cross-linking agent (curve b), MNZ antibody (curve c), BSA (curve d) and MNZ (0.25 μM, curve e) onto the modified electrode surface, the corresponding photocurrent responses also gradually diminished with each modification step (Fig. 3B), consistent with the results of EIS, also indicating the successful construction of the present PEC immunoassay.

3.3. Optimization of experimental parameters

During the PEC measurements, the amount of photoactive material was firstly optimized. The photocurrent initially increases with the amount of the cg-C_3N_4 dispersion up to 30 μL and then decreases (Fig. 4A), likely due to the presence of the nanostructured cg-C_3N_4 on the electrode. With the presence of more cg-C_3N_4, more electron-hole pairs could take part in the PEC process. With the amount of cg-C_3N_4 further increased, the aggregation of the nanostructures occurred and the coated thicker film may hinder electron transfer, thus leading to the

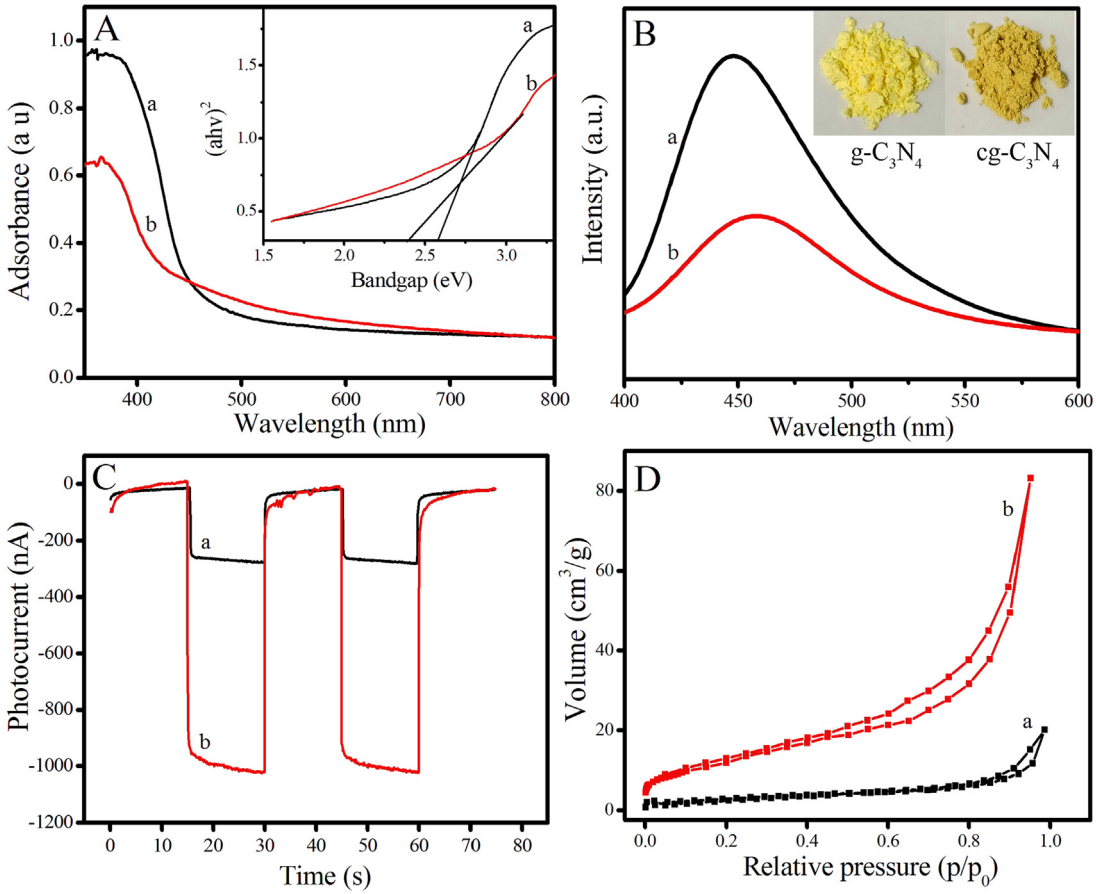

Fig. 2. (A) The UV–vis diffuse reflectance spectra of (a) g-C_3N_4, (b) cg-C_3N_4 (Inset: linear fitting to Tauc's reported curves); (B) Photoluminescence spectra of (a) g-C_3N_4 and (b) cg-C_3N_4 excited by 365 nm (Inset: optical photographs of the as-prepared g-C_3N_4 and cg-C_3N_4); (C) Photocurrent responses and (D) N_2 adsorption–desorption isotherms of (a) g-C_3N_4 and (b) cg-C_3N_4.

decrease of PEC response. Meanwhile, the thicker film may also be easily peeled off from the electrode surface (Fang et al., 2016). Therefore, the optimal amount of cg-C_3N_4 dispersion is 30 μL.

The concentration of the hole sacrificial agent was also closely related with the PEC response. The photocurrent response increased with the concentration of AA up to 0.1 M and then remained steady due to the saturation of AA as electron donor (Fig. 4B). Thus, the optimum concentration of AA is 0.1 M.

Because the pH of the detection solution not only affects the PEC responses of the immunoassay, but also the activity of the immobilized proteins, the pH effect on the PEC response was investigated within the range of 5.0–9.0 in the detection solution (in the presence of 0.1 M AA). A maximum photocurrent response was investigated at pH 7.0 (Fig. 4C). Thus, the optimal pH value of 7.0 was selected in the further

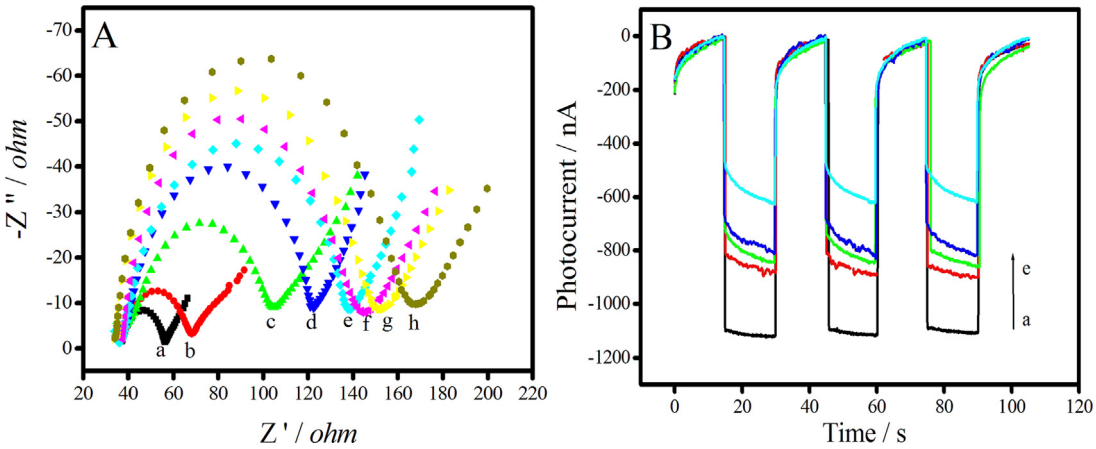

Fig. 3. (A) EIS of (a) FTO foil, (b) cg-C_3N_4/FTO, (c) GLD-CS/cg-C_3N_4/FTO, (d) Ab/GLD-CS/cg-C_3N_4/FTO, (e) BSA/Ab/GLD-CS/cg-C_3N_4/FTO, and (f-h) MNZ/BSA/Ab/GLD-CS/cg-C_3N_4/FTO (corresponding to the different concentration of MNZ from f to h: 0.01, 0.25 and 1.0 μM) in the presence of 2.5 mM $K_3[Fe(CN)_6]/K_4[Fe(CN)_6]$ (1:1) in 0. 1 M PBS. The applied frequency in the range of 0.1 Hz–100 kHz; (B) Corresponding photocurrents of cg-C_3N_4/FTO after each step decoration with on-off illumination under visible light (from a to e, cg-C_3N_4/FTO, GLD-CS/cg-C_3N_4/FTO, Ab/GLD-CS/cg-C_3N_4/FTO, BSA/Ab/GLD-CS/cg-C_3N_4/FTO, and MNZ/BSA/Ab/GLD-CS/cg-C_3N_4/FTO). Supporting electrolyte: 0.1 M pH 7.0 tris–HCl.

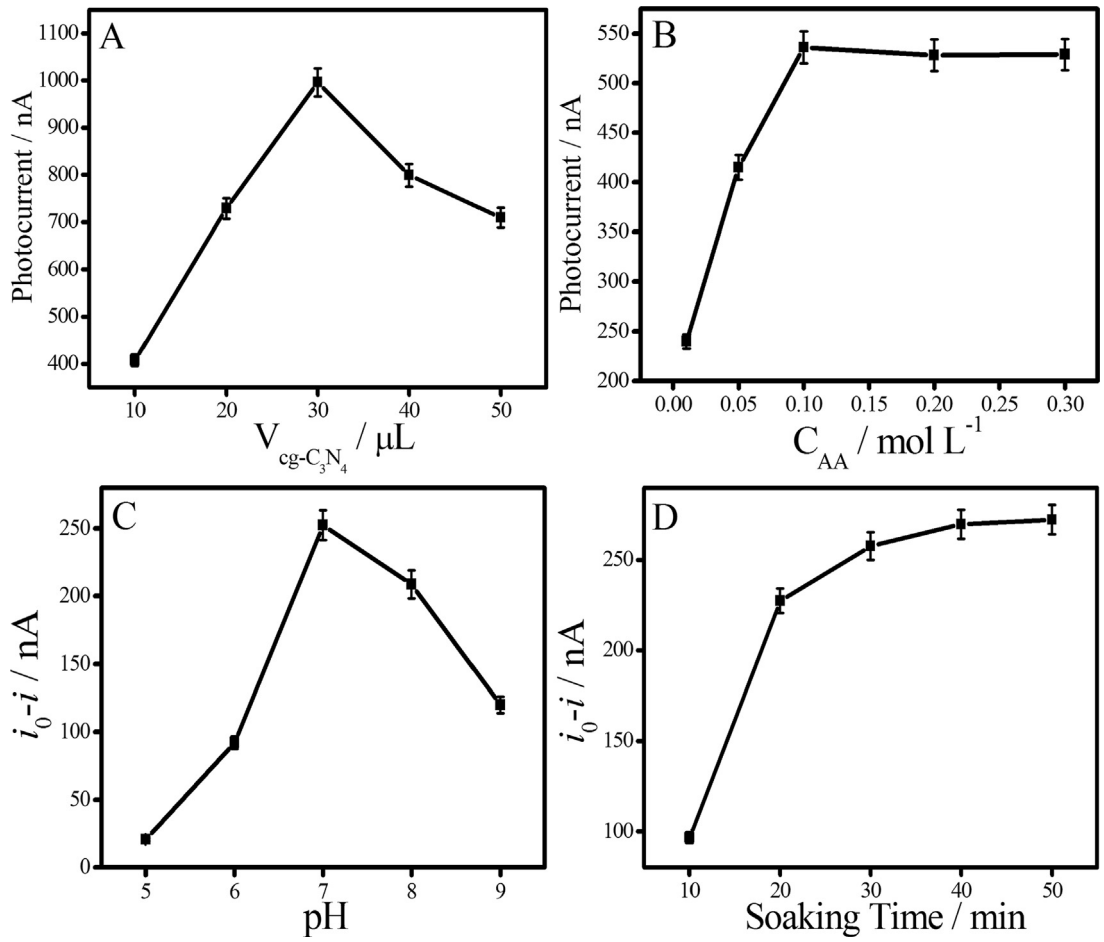

Fig. 4. Effects of (A) the volume of cg-C_3N_4 pre-cast onto FTO on the photocurrent responses of cg-C_3N_4/FTO; (B) the concentration of hole sacrificial agent of AA; (C) pH value of the buffer solution tris–HCl; (D) immersion time on the photocurrents of BSA/Ab/GLD-CS/cg-C_3N_4/FTO into MNZ (0.25 μM) solution. Supporting electrolyte: 0.1 M pH 7.0 tris–HCl.

study.

As an influential parameter, the dependence of the PEC immunoassay on the incubation time was examined (Fig. 4D). With prolonging incubation time in MNZ solution, the photocurrents increased rapidly up to 30 min, then became smooth and remained stable. With the incubation time greater than 30 min, the immuno-binding interactions tended to be saturated. Hence, for the incubation steps, the optimum time is 30 min.

3.4. Analytical performance of the Present PEC immunoassay

Under the optimized conditions, the photocurrent responses of the proposed cg-C_3N_4-based PEC immunosensor were investigated in the presence of varied concentrations of MNZ (shown in Fig. 5A). With the successive entrapment of MNZ, the induced steric hindrance hampered the diffusion of AA (hole sacrificial agent) to the electrode surface to capture photogenerated holes. Thus, the produced photocurrent of sensor decreased successively with the increase of MNZ concentrations in the immersion solution. The relative change of the photocurrent, expressed as $(i_0\text{-}i)/i_0$ (where i_0 and i correspond to the photocurrent before and after incubation in MNZ) toward the logarithm value of MNZ concentrations displays a linear relationship over the linear dynamic range of 0.01–100 μM (inset of Fig. 5A). The corresponding linearization equation is: $(i_0\text{-}i)/i_0 = 0.195 + 0.491 \log c/\mu mol\ L^{-1}$. The estimated detection limit is calculated to be 0.005 μM at signal to noise ratio of 3, significantly lower than the previous reports (Table S1). Thus, such distinguished analytical performance is sufficient to monitor MNZ levels in real sample analysis.

3.5. Selectivity and stability of the PEC sensor

To evaluate the specificity of the present PEC sensor towards MNZ, several analogs of MNZ (Table S2), were selected as possible interferents. It can be found that the responses to the interfering agents alone were close to that of the blank signal (Fig. 5B). In the two-component system, including MNZ and each individual interference with equal concentration of 0.25 μM, the photocurrent of PEC sensor is almost unchanged in comparison with that of MNZ alone. Even in the presence of the interfering compound with 20-fold concentration of MNZ, all the changes of the photocurrent are less than 11.4%. All measurement values for each interfering compound show consistence well with acceptable precision (% RSDs = 1.2–8.1%, n = 3). These data show that the present PEC biosensor presents high selectivity and repeatability. Operational stability is also a key factor to be investigated in practical applications. In the initial 3 days, the photocurrent response of MNZ was almost unchanged. After 7 days (stored at 4 °C all the time), the sensor retained about 96.0% of its initial response (Fig. S1), displaying a good stability.

3.6. Analysis of the real oral medicine samples

The practical application of the present PEC sensor was further studied for the determination of MNZ in actual oral medicine samples. Two kinds of MNZ tablets with SDA No. H10980058 (labeled to contain

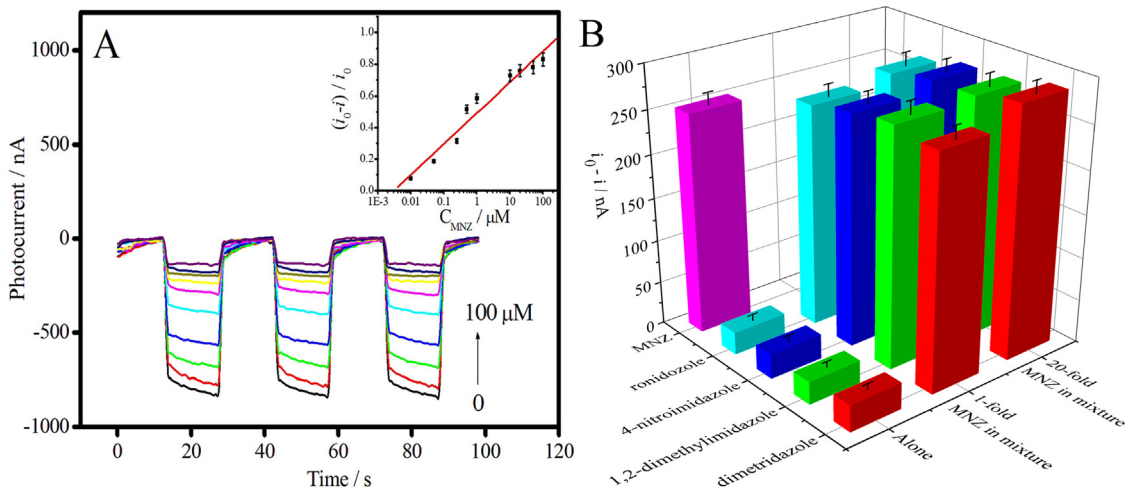

Fig. 5. (A) PEC profile ofthe present immunoassay toward different concentraitons of MNZ (from bottom to top, 0, 0.01, 0.05, 0.25, 0.5, 1.0, 10, 20, 50 and 100 μM). Inset: the calibration curve of the PEC inhibition ratio against the concentration of MNZ; (B) The evaluation of specificity of the proposed PEC immunoassay to the interfering substances: dimetridazole, 1,2-dimethylimidazole, 4-nitroimidazole, ronidazole, and their mixture with different folds concentration to MNZ (0.25 μM). Supporting electrolyte: 0.1 M pH 7.0 tris–HCl.

Table 1
PEC Determination of MNZ in Different Serum Samples using the Proposed Method (n = 3).

Sample	Concentration		Recovery (%)
	Taken (ng mL^{-1})	Found (ng mL^{-1})	
Sample 1	0.0	0.0178	———
Sample 1-1	1.00	0.997	99.7
Sample 1-2	5.00	4.477	89.5
Sample 2	0.0	1.207	———
Sample 2-1	10.0	9.772	97.7
Sample 2-2	50.0	53.21	106.4

3 mg MNZ per tablet) and H41024459 (labeled as 0.2 g MNZ per tablet) were collected for real sample analysis, respectively. For the preparation of the stock solutions, each tablet was first grinded into powder and then transferred into 1000 mL volumetric flask using ultrapure water as solvent, respectively. Finally, the as-prepared stock solutions were diluted 1000 folds with water, and then carried out the measurements using the present immunoassay (listed in Table 1). The recoveries of MNZ in the oral medicine samples were found to be in the range of 89.5–106.4%. Using the proposed PEC immunoassay, the original contents of MNZ in the oral medicine samples were detected to be 0.0178 μM (equivalent to 3.04 mg MNZ per tablet) and 1.207 μM (equivalent to 0.206 g MNZ per tablet), respectively, completely agreeing well with the labeled values. Obviously, the proposed method occupies a high degree of sensitivity, accuracy, reproducibility and applicability for direct analyzing real samples. And moreover, the analysis progress by the present PEC sensor is simpler, rapider, and more low-cost.

4. Conclusions

In summary, this work first exploited the use of cg-C_3N_4 incorporated with immunoassay technology for PEC sensing MNZ. The unique coral-like g-C_3N_4 nanoarchitectures greatly facilitate the photogenerated electron-hole separation and provide more active sites for grafting capture antibodies, thus amplifying the photocurrent response. The resulting PEC immunoassay displays excellent performance for MNZ determination with a linear range of 0.01–100 μM and a detection limit of 0.005 μM (S/N = 3). It has been proved to be applicable for sensing MNZ in common oral medicine samples. This protocol eliminates the need for sophisticated instruments and high detection expenses, making it possible to be a reliable alternative in resource–constrained regions. The further work is undergoing to explore the present protocol for real pharmaceutical analysis.

Acknowledgements

This work was supported by National Natural Science Foundation of China (Grant 21475050, 21777052), and Self-determined Research Funds of Central China Normal University (CCNU) from the Colleges' Basic Research and Operation of MOE (CCNU18TS013).

Appendix A. Supporting information

Supplementary data associated with this article can be found in the online version at doi:10.1016/j.bios.2018.09.084.

References

Ardsoongnearn, C., Boonbanlu, O., Kittijaruwattana, S., Suntornsuk, L., 2014. J. Chromatogr. B 945–946, 31–38.
Chen, D., Deng, J., Liang, J., Xie, J., Hu, C., Huang, K., 2013. Sens. Actuators B183, 594–600.
Chen, S., Li, A., Zhang, L., Gong, J., 2015. Anal. Chim. Acta 896, 68–77.
Cui, Y., Ding, Z., Fu, X., Wang, X., 2012. Angew. Chem. Int. Ed. 51, 11814–11818.
Dai, H., Zhang, S., Hong, Z., Lin, Y., 2016. Anal. Chem. 88, 9532–9538.
Duan, J., Zhang, Y., Yin, Y., Li, H., Wang, J., Zhu, L., 2018. Sens. Actuators B 257, 504–510.
Fan, D., Bao, C., Khan, M.S., Wang, C., Zhang, Y., Liu, Q., Zhang, X., Wei, Q., 2018. Biosens. Bioelectron. 106, 14–20.
Fang, T., Yang, X., Zhang, L., Gong, J., 2016. J. Hazard. Mater. 312, 106–113.
Gao, C., Wang, Y., Yuan, S., Xue, J., Cao, B., Yu, J., 2017. Biosens. Bioelectron. 90, 336–342.
Ge, L., Wang, Y., Yang, H., Yang, P., Cheng, X., Yan, M., Yu, J., 2014. Anal. Chim. Acta 828, 27–33.
Han, Q., Wang, R., Xing, B., Chi, H., Wu, D., Wei, Q., 2018. Biosens. Bioelectron. 106, 7–13.
Hou, Y., Laursen, A.B., Zhang, J., Zhang, G., Zhu, Y., Wang, X., Dahl, S., Chorkendorff, I., 2013. Angew. Chem. Int. Ed. 52, 3621–3625.
Jin, W.R., Dong, Q., Yu, D.Q., Ye, X.Y., Li, W., 2000. Electrophoresis 21, 1540–1544.
Jun, Y.S., Lee, E.Z., Wang, X., Hong, W.H., Stucky, G.D., Thomas, A., 2013. Adv. Funct. Mater. 23, 3661–3667.
Korany, M.A., Abdine, H.H., Ragab, M.A., Aboras, S.I., 2015. Spectrochim. Acta A 143, 281–287.
Li, H., Li, J., Zhu, Y., Xie, W., Shao, R., Yao, X., Gao, A., Yin, Y., 2018. Anal. Chem. 90, 5496–5502.
Li, R., Zhang, Y., Tu, W., Dai, Z., 2017. ACS Appl. Mater. Interfaces 9, 22289–22297.
Li, X., Wang, X.L., Zhang, L.Z., Gong, J.M., 2018. ACS Sens. 3, 1480–1488.
Liang, Q., Li, Z., Huang, Z.H., Kang, F., Yang, Q.H., 2015. Adv. Funct. Mater. 25, 6885–6892.

Liao, G., Chen, S., Quan, X., Yu, H., Zhao, H., 2012. J. Mater. Chem. 22, 2721–2726.
Liu, G., Qiao, X., Gondal, M.A., Liu, Y., Shen, K., Xu, Q., 2018. J. Nanosci. Nanotechnol. 18, 4142–4154.
Liu, L., Lv, H., Wang, C., Ao, Z., Wang, G., 2016. Electrochim. Acta 206, 259–269.
Lu, Q., Deng, J., Hou, Y., Wang, H., Li, H., Zhang, Y., 2015. Chem. Commun. 51, 12251–12253.
Lu, Z., Zeng, L., Song, W., Qin, Z., Zeng, D., Xie, C., 2017. Appl. Catal. B 202, 489–499.
Ma, W., Han, D., Zhou, M., Sun, H., Wang, L., Dong, X., Niu, L., 2014. Chem. Sci. 5, 3946–3951.
Mahrouse, M.A., Elkady, E.F., 2011. Chem. Pharm. Bull. 59, 1485–1493.
Mehrzad-Samarin, M., Faridbod, F., Dezfuli, A.S., Ganjali, M.R., 2017. Biosens. Bioelectron. 92, 618–623.
Moussa, B.A., El-Kady, E.F., Mohamed, M.F., Youssef, N.F., 2017. J. Planar Chromat. 30, 481–487.
Ong, W.J., Tan, L.L., Ng, Y.H., Yong, S.T., Chai, S.P., 2016. Chem. Rev. 116, 7159–7329.
Schkarpetkin, D., Reise, M., Wyrwa, R., Volpel, A., Berg, A., Schweder, M., Schnabelrauch, M., Watts, D.C., Sigusch, B.W., 2016. Dent. Mater. 32, 951–960.
Shen, Q., Han, L., Fan, G., Zhang, J.R., Jiang, L., Zhu, J.J., 2015. Anal. Chem. 87, 4949–4956.
Shu, J., Qiu, Z., Lin, Z., Cai, G., Yang, H., Tang, D., 2016. Anal. Chem. 88, 12539–12546.
Song, H., Zhang, L., Yu, F., Ye, B.C., Li, Y., 2016. Electrochim. Acta 208, 10–16.
Sun, G., Zhang, Y., Kong, Q., Zheng, X., Yu, J., Song, X., 2015. Biosens. Bioelectron. 66, 565–571.
Thompson, C.S., Traynor, I.M., Fodey, T.L., Crooks, S.R., 2009. Anal. Chim. Acta 637, 259–264.
Wang, K., Li, Q., Liu, B., Cheng, B., Ho, W., Yu, J., 2015. Appl. Catal. B 176–177, 44–52.
Wang, Y., Ge, S., Zhang, L., Yu, J., Yan, M., Huang, J., 2017. Biosens. Bioelectron. 89, 859–865.
Wang, Y., Zhang, P., Jiang, N., Gong, X., Meng, L., Wang, D., Ou, N., Zhang, H., 2012. J. Chromatogr. B 899, 27–30.
Xie, M., Wei, W., Jiang, Z., Xu, Y., Xie, J., 2016. Ceram. Int. 42, 4158–4170.
Xie, Z., Feng, Y., Wang, F., Chen, D., Zhang, Q., Zeng, Y., Lv, W., Liu, G., 2018. Appl. Catal. B 229, 96–104.
Yang, S., Gong, Y., Zhang, J., Zhan, L., Ma, L., Fang, Z., Vajtai, R., Wang, X., Ajayan, P.M., 2013a. Adv. Mater. 25, 2452–2456.
Yang, Y., Guo, Y., Liu, F., Yuan, X., Guo, Y., Zhang, S., Guo, W., Huo, M., 2013b. Appl. Catal. B 142–143, 828–837.
Ye, C., Li, J.X., Li, Z.J., Li, X.B., Fan, X.B., Zhang, L.P., Chen, B., Tung, C.H., Wu, L.Z., 2015. ACS Catal. 5, 6973–6979.
Yu, J., Wang, K., Xiao, W., Cheng, B., 2014. Phys. Chem. Chem. Phys. 16, 11492–11501.
Yue, D., Qian, X., Kan, M., Fang, M., Jia, J., Yang, X., Zhao, Y., 2018. Appl. Catal. B 229, 211–217.
Zhao, W.W., Yu, P.P., Shan, Y., Wang, J., Xu, J.J., Chen, H.Y., 2012. Anal. Chem. 84, 5892–5897.
Zheltvai, O.I., Zheltvai, I.I., Spinul, V.V., Antonovich, V.P., 2013. J. Anal. Chem. 68, 600–605.
Zheng, Y., Lin, L., Ye, X., Guo, F., Wang, X., 2014. Angew. Chem. Int. Ed. 53, 11926–11930.